



Effect of Obstacle Configuration in Sinusoidal BFSC on Hydrothermal Performance and Irreversibility Characteristics: A Numerical Study

Brajesh Kumar Kanchan^{1,2} · Guddakesh Kumar Chandan¹ · Jyoti Kumar³

Received: 19 February 2022 / Accepted: 19 March 2023 / Published online: 31 May 2023
© The Author(s), under exclusive licence to Shiraz University 2023

Abstract

The present investigation discusses the influence of obstacle configurations on the hydrothermal and irreversibility characteristics of a sinusoidal backward-facing step channel. The study investigates the interplay of obstacle configuration, namely profiles, locations, and orientations. Different obstacle profiles of identical areas, including square, rhomboid, triangular, circular, and elliptical, are studied. Nusselt number, pressure drop, irreversibility, and hydrothermal factor are the output parameters. Our results highlight that the reattachment length decreases because of the obstacle placed near the channel's inlet, independent of the obstacle's geometrical configuration. Further, the recirculation zone length is found to be the smallest for the square obstacle. The local Nusselt number is found to be greatest at the location of the obstacle, and the peak value of the local Nusselt number is greatest for the backward-facing step channel with a rhomboid obstacle. It was observed that the average Nusselt number, pressure drop, and irreversibility characteristics all increase with the increase in Richardson number irrespective of the shape of the obstacle, and are greatest in the case of a triangular obstacle. However, the elliptical obstacle has a higher hydrothermal factor, indicating that it has the optimum obstacle geometry. In addition, elliptical obstacles with step obstruction distance along the x and y axis, namely ($L_x = 10$ and $L_y = 2.2$), ($L_x = 20$ and $L_y = 2.2$), are considered as optimal obstacle locations. The angular orientation of 0° is found to have the maximum hydrothermal factor. These findings demonstrate the interplay of wall-obstacle architecture on hydrothermal and irreversibility performance and highlight their importance as a design feature.

Keywords Obstacle · Mixed convection · Backward-facing step · Nusselt number · Irreversibility

1 Introduction

The recent past has seen an upsurge in the research on heat transfer enhancement owing to its applications in combustors (Feng et al. 2023; Zhang et al. 2022; Yan et al. 2021), diffusers (Kumar et al. 2022; Bekhradinasab et al. 2021; Guo et al. 2021), turbines (Jin et al. 2022; Xing et al. 2022; Shen and Wang 2022), heat exchangers (Geng et al. 2023; Khattoon et al. 2022; Ali et al. 2022), and cooling of electronic

systems (Warrier et al. 2012; Kannan and Kamatchi 2020). The probing of backward-facing step channels (BFSC) has increased in the last decade to illustrate flow separation and reattachment. Most of the studies in this context have been carried out for the type of flow, orientation of BFSC (Boruah et al. 2018; Soong and Hsueh 1993; Abu-Mulaweh et al. 1995; Barton 1998), passive modes for heat enhancement (Nie et al. 2009; Heshmatian and Bahiraei 2017; Tropea and Gackstatter 1985; Oztop and Al-Salem 2012; Korichi and Oufer 2007), and entropy generation (Heshmatian and Bahiraei 2017; Bahiraei et al. 2017; Najafi Khaboshan and Nazif 2019) applying various boundary conditions and assumptions. Further, the obstacles at the channel entrance significantly alter flow physics (Zeeshan et al. 2016; Mehrez et al. 2009; Nouri-Borujerdi and Moazezi 2018; Tzeng et al. 2007; Yojina et al. 2010). The surface waviness also disturbs the flow and enhances the convection mechanism to add complexity. A detailed understanding of the influence of obstacle configurations (geometry, orientation, and locations) and

✉ Brajesh Kumar Kanchan
brajeshlean@gmail.com

¹ Department of Mechanical Engineering, National Institute of Technology Silchar, Silchar, Assam 788010, India

² Department of Production Engineering, PSG College of Technology, Coimbatore, Tamilnadu 641004, India

³ Department of Mechanical Engineering, Government Engineering College Khagaria, Aryabhata Knowledge University, Khagaria, Bihar 848203, India

the waviness of the surface on thermohydraulic transport characteristics is essential to quantify the extent of thermal enhancement was missing in the present literature. Hence, an attempt is made to present a detailed investigation of obstacle configurations on hydrothermal and irreversibility characteristics.

Several investigators have worked on thermohydraulic characteristics related to BFSC for laminar, transitional, and turbulent flow regimes. Soong and Hsueh (1993) studied the effect of cold flow injection on the heat transfer rate and reported that the injection of cold fluid enhances the rate of heat transfer. They further proposed a bilinear correlation for the accurate prediction of reattachment length. Xie et al. (2017) numerically simulated vortices on the bottom wall and their impact on heat transfer in BFSC. They reported that heat transfer significantly enhances transitional Reynolds number (Re) in the range of $6 \leq \text{streamwise coordinate/channel height} \leq 14$. Barton (1998) scrutinized the entrance effects of the flow for low and high Re and observed that a significant difference occurred for low Re . He also concluded that low expansion numbers of channels experienced a higher entrance effect after some interval, irrespective of any sudden expansion stream. Avancha and Pletcher (2002) examined the heat transfer and fluid characteristics for BFSC through large eddy simulations and noted a temperature increase near step geometry. The effect of the orientation of BFSC has been studied extensively for horizontal, inclined, and vertical directions. Taher et al. (2018) worked on capillary flow in BFSC for microchannel and reported an aspect ratio of 0.5–3. Iwai et al. (2000) analyzed the impact of pitch and rolling angle of BFSC. They delineated that the buoyancy effect appears to be insignificant for horizontal flows. Lin et al. (Lin et al. 1990) investigated vertical BFSC and correlated the buoyancy with reattachment length.

Several researchers in the literature focused on the type of flow, such as natural, mixed convection, and forced, with BFSC. Boruah et al. (2018) analyzed different baffles mounted on an adiabatic wall and reported that an elliptical baffle has superior performance compared to other baffles, namely square or triangular, for thermohydraulic and entropy generation characteristics. They further worked on step distances and concluded that total irreversibility is smaller for a larger step distance between the baffle and axis. Tropea and Gackstatter (1985) compared a fence flow with blockage flow and reported that low blockage ratios generated longer reattachment lengths consistently in the fence geometry. They also noted that the obstacle results in longer reattachment lengths at higher blockage ratios. Öztöp et al. (2012) numerically analyzed double forward-facing steps with obstacles in the turbulence model. They noted that the heat transfer rate is a function of the obstacle's aspect ratio and step height. Abu et al. (2006) investigated natural convection in vertical BFSC and noted a relation between

temperature gradient and friction coefficient. Saldana et al. (2005) studied a 3D numerical study in BFSC for mixed convection. They concluded that the average Nusselt number (Nu) peak moves upstream with an increase in Ri . Al-aswadi et al. (2010) worked in laminar forced convection and noted that the reattachment region shifts downstream as the magnitude of Re increases. Applying various passive modes in fluid flow has been instrumental in enhancing heat transfer since it results in a variation of the flow field. In this context, several geometrical configurations include the insertion of baffles, porous cavities, and obstacles. Selimefendigil and team worked on the interplay of convection and backward-facing steps using nanoparticles and a magnetic field for thermohydraulic characteristics. Selimefendigil et al. (2019) noted that heat transfer improved by 14% once pulsating flow and the magnetic dipole were used. In another work, Kolsi et al. (2021) reported an improvement in local and average heat transfer using nanoparticles and an inclined magnetic field. The average Nusselt number acts as the decreasing function for the Strouhal number (Chamkha and Selimefendigil 2018). Moreover, the nanoparticle improved heat transfer performance by 52% at its maximum fraction (Selimefendigil and Öztöp 2020). Additionally, heat transfer performance is highest for circular shapes, which is 7.45% higher when nanoparticles are used (Selimefendigil and Öztöp 2016). The sinusoidal wave channel improves thermal performance mixing and other characteristics, making it suitable for mixing applications and energy conversion technology such as fuel cell devices (Chang et al. 2009; Beigzadeh and Ozairy 2019; Ma et al. 2021; Zhou et al. 2022; Ghasemi et al. 2021; Anyanwu et al. 2019). Ghasemi et al. (2021) studied sinusoidal channels and reported an increase in thermophoresis and temperature distribution. Chang et al. (2009) concluded that wave channels improved heat performance owing to the generation of vortices.

In a thermal system, irreversibility deteriorates the system performance, which can be quantified through the rate of entropy generation (Bejan 1998). Hence, several investigators studied entropy generation to optimize system effectiveness. In this context, Zeeshan et al. (2016) studied the shape effect of nanoparticles over entropy generation. They concluded that proper nanoparticle choice could control velocity profile and heat transfer, and irreversibility could be reduced by utilizing the property of nanofluids containing spherical particles. Mahian (2013) examined the entropy generation in nanofluids, concluding that nanofluids contribute to decreasing entropy generation and overall system optimization. Baytas (1999) worked with porous cavities and entropy generation in natural convection. He found that heat transfer irreversibility dominated over friction irreversibility as the Rayleigh number (Ra) decreased.

Despite numerous investigations, as outlined above, the irreversibility aspects are largely missing in the literature.

Moreover, the interplay of sinusoidal wave and BFSC has not been studied explicitly for thermohydraulic and irreversibility characteristics. Furthermore, there are no comprehensive studies wherein the implication of fundamental obstacle geometries, namely triangular, square, rhomboid, circular, or elliptical configurations, are compared in a sinusoidal wave integrated backward-facing step channel for hydrothermal and irreversibility characteristics to obtain the optimal obstacle. Additionally, a detailed study on the influence of obstacle location and angular inclination has not been conducted. Therefore, to bridge this literature gap, the present investigation aims to conduct a thorough analysis and investigate the implication of obstacle shape, space, and angular inclination for a sinusoidal integrated backward-facing step channel. These findings demonstrate the interplay of wall-obstacle architecture on hydrothermal and irreversibility performance and highlight their importance as a design feature.

2 Formulation

This study investigates the effect of different obstacle geometries on heat transfer and fluid flow characteristics for mixed convection in a backward-facing step channel (BFSC). A sinusoidal heat wall is configured after BFSC

for fully developed flow, as depicted in Fig. 1a. Figure 1b illustrates the different obstacle configurations at point A, and the angular orientation of the elliptical obstacle is shown in Fig. 1c.

Obstacles of different geometrical configurations with equal surface area are placed at the inlet of the BSFC. The surface of the bottom wall and obstacle is kept at a high temperature (T_h), and the temperature of the fluid is equal to T_o ($< T_h$). The top wall of the channel is assumed to be adiabatic. Air is taken as the working fluid for the investigation with a Prandtl number equal to 0.71. Two-dimensional, laminar, incompressible, and Newtonian fully developed flow are considered. Viscous dissipation and radiation heat transfer are neglected. The operating range Richardson number (Ri) is 0.05–1, and the Reynolds number (Re) is constant at 100. It can be noted that the Reynolds number is the ratio of inertial force to viscous force, whereas the Richardson number is the ratio of the buoyancy term to the flow shear term. The non-dimensional parameters used in the current study are shown in Table 1. A separate investigation is carried out to understand the effect of the location and orientation of obstacles on heat transfer characterized using elliptical obstacles. In this context, the obstacle-to-step obstruction distance is varied. The obstacle is placed at $L_x = (1, 5, 10, 20, 30, \text{ and } 39)$ and $L_y = (0.7, 1.0, 1.3, 1.6, 2.2, \text{ and } 2.5)$ for the study.

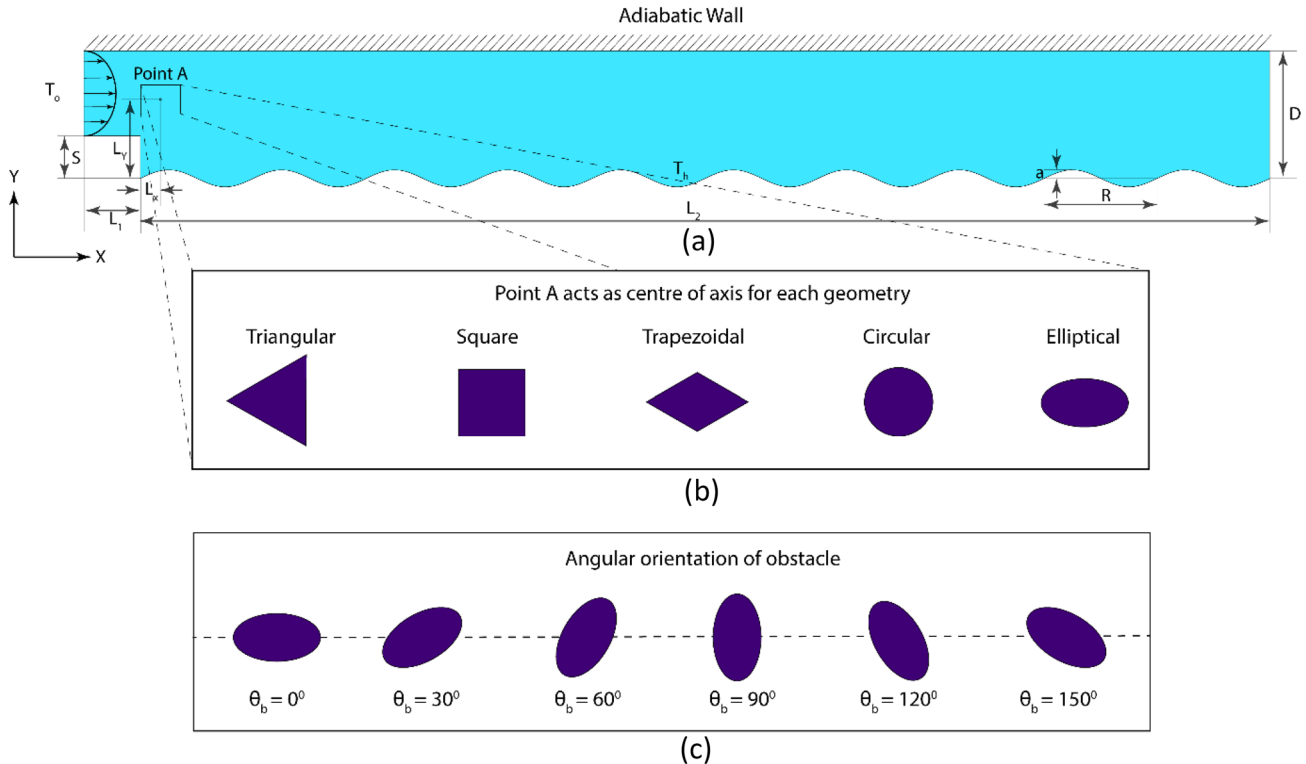


Fig. 1 Schematic of the BFSC with the sinusoidal bottom heated wall for (a) no obstacle configuration, (b) different geometrical configurations at point A, and (c) angular orientation of elliptical obstacle

Table 1 Non-dimensional parameters and their values

d	E	L_1	L_2	S	L_x	L_y	θ_b
3	1.5	2	12.33D	0.886	1,5,10,20,30,39	0.7,1,1.3,1.6,1.9,2.2	0°,30°,60°,90°,120°,150°

The elliptical obstacles are positioned at inclination angles (θ_b) of 0°, 30°, 60°, 90°, 120°, and 150° to understand the influence of the angle of obstacles on heat transfer characteristics. It can be noted that the inclination angle is the obstacle orientation with respect to the flow axis, as shown in Fig. 1c. The pre-expansion length (L_1) and post-expansion length (L_2) are shown in Table 1 (refer to Fig. 1a).

It can be noted that d , E , and S are dimensionless height, expansion ratio, and step height, respectively.

2.1 Governing Equations

The three governing equations involved in the present study are continuity, momentum, and energy and are presented below.

Mass conservation:

$$\nabla \cdot V = 0 \quad (1)$$

Momentum conservation:

$$V \cdot \nabla V = -\nabla P + \frac{1}{\text{Re}} \nabla^2 V + \frac{Gr}{\text{Re}^2} \theta \quad (2)$$

Energy conservation:

$$V \cdot \nabla \theta = \frac{1}{\text{PrRe}} \nabla^2 \theta \quad (3)$$

where the following non-dimensionalized parameters are used.

$$(X, Y) = \frac{(x, y)}{S}, V = \frac{v}{U_0}, P = \frac{p}{\rho U_0^2}, \theta = \frac{T - T_0}{T_H - T_0}, \text{Re} = \frac{\rho U_0 S}{\mu}, \text{Pr} = \frac{\mu C_p}{k}, Gr = \frac{g \beta \Delta T S^3}{\nu^2} \quad (4)$$

where X , Y , U_0 are Cartesian coordinates and average inlet velocity, respectively. All other notations have their usual meaning (Boruah et al. 2018).

System irreversibility (N_{Total}) is expressed as

$$N_{\text{Total}} = N_{\text{Thermal}} + N_{\text{Viscous}} \quad (5)$$

$$N_{\text{Total}} = \left[\left(\frac{\partial \theta}{\partial X} \right)^2 + \left(\frac{\partial \theta}{\partial Y} \right)^2 \right] + \left[\frac{1}{\text{Re}} \left\{ 2 \left(\left(\frac{\partial \theta}{\partial X} \right)^2 + \left(\frac{\partial \theta}{\partial Y} \right)^2 \right) + \left(\frac{\partial U}{\partial Y} + \frac{\partial V}{\partial X} \right)^2 \right\} \right] \quad (6)$$

The Bejan number (Be) is the ratio of thermal entropy to total entropy (Boruah et al. 2018)

$$Be = \frac{N_{\text{Thermal}}}{N_{\text{Total}}} \quad (7)$$

2.2 Boundary Conditions

The boundary conditions consist of defined parametric values for the computational domain, which comprises a channel inlet, channel outlet, geometric wall, and obstacle wall.

Channel inlet

$$U = 1.5 * U_0 * (Y - 1)(3 - Y) \quad (8)$$

Channel outlet

$$\frac{\partial U}{\partial X} = \frac{\partial V}{\partial X} = \frac{\partial \theta}{\partial X} = 0 \quad (9)$$

Geometric wall

Upper wall

$$U = V = \frac{\partial \theta}{\partial Y} = 0 \quad (10)$$

Sinusoidal wall

$$U = V = 0; \theta = 1 \quad (11)$$

Obstacle wall

$$U = V = \frac{\partial \theta}{\partial n} = 0 \quad (12)$$

3 Numerical Method and Grid Independence

The numerical methods represent the computational methodology adopted herein. First, mass, momentum, and energy conservation equations are computed using the finite element method. Laminar flow and heat transfer in fluids are used together as solutions in the present study. The Galerkin weighted residual method is used to solve the governing equations with boundary conditions. The independent variables, temperature, pressure, and velocity profiles, are analyzed. Conjugate gradient iterative methods in the form of a PARDISO direct solver is considered with convergence criteria of 10^{-8} .

Before starting the analysis, it is essential to select an optimized mesh size through a grid sensitivity test for all geometrical configurations. Each geometry has four grid

sizes for this study. The average Nusselt number is calculated for the studied obstacle configurations for various elements at $Ri = 0.05$, $Re = 25$, as shown in Table 2. It can be noted that \overline{Nu} does not change significantly from mesh elements 151,831 to 363,747 for circular obstacles, resulting in a variation of 0.09%. Therefore, a trade-off is considered between computational accuracy and time. Hence, mesh elements of 151,831 are chosen for the circular obstacle. Similarly, channels with elliptical, triangular, square, and rhomboid obstacle mesh sizes with 151,745, 157,277, 158,187, and 157,705 elements, respectively, are chosen.

4 Model Validation

Before presenting the results of the present study, the in-house codes must be compared with the available literature to check the code's accuracy. The literature selected to compare numerical codes is the work of Boruah et al. (2018), as the author worked on different baffle configurations in backward-facing step channels and determined the hydrothermal and irreversibility features for $Re = 100$ and Ri between 0.05 and 1. Boruah et al. (2018) analyzed different baffles mounted on an adiabatic wall and reported that an elliptical baffle performs superior to other baffles, namely square and triangular, for thermohydraulic and entropy generation features. They further worked on step distances and concluded that total irreversibility is smaller for a larger step distance between the baffle and axis. The Nusselt number is compared between in-house codes, and the plot of Boruah et al. (2018) is shown in Fig. 2a. Furthermore, the experimental data of Abu-Mulaweh et al. (1993) is also compared to evaluate the computational accuracy, as illustrated in Fig. 2b. It can be spotted that there is no significant difference found in plots and thus validated the codes for the current study.

5 Results and Discussion

The present study discusses the influence of the obstacle's configuration and orientation on the hydrothermal and irreversibility characteristics in a backward-facing step channel (BFSC). In the current work, obstacles with triangular, square, rhomboid, circular and elliptical shapes have been placed near the inlet of the BFSC. The Reynolds number is kept constant at 100, whereas the Richardson number varies from 0.05 to 1. In the subsequent sections, the results are expressed in streamline contour, isotherms, Nusselt number, pressure drop, Bejan number, and irreversibility characteristics. The inference obtained from streamlines and isotherms, Nusselt number, and Bejan number over the entire length of BFSC illustrate the impact of using different obstacles on these parameters. Furthermore, the average Nusselt number, pressure drop, irreversibility against Richardson number (0.05–1), and Reynolds number (100) demonstrate the effect of obstacle geometry, orientation and location characteristics.

5.1 Effect of the Obstacle Geometry

It is already well known that the insertion of obstacle geometry generates recirculation and flow reattachment, which ultimately enhances heat transfer (Tropea and Gackstatter 1985). Hence, a comparative analysis has been conducted to gain insight into the influence of the geometrical configuration of obstacles on \overline{Nu} , ΔP , and N_{Total} . The obstacles at the inlet of the channel with triangular, square, rhomboid, circular, and elliptical shapes have been considered for the present investigation.

Table 2 Average Nusselt number comparison for grid independence study

Circular obstacle			Elliptical obstacle			Triangular obstacle		
No. of elements	\overline{Nu}	% error	No. of elements	\overline{Nu}	% error	No. of elements	\overline{Nu}	% error
26,223	1.966	1.32	26,389	1.803	1.27	27,776	1.657	4.38
63,510	1.982	0.53	63,510	1.819	0.44	66,422	1.702	1.80
151,831	1.990	0.09	151,745	1.826	0.03	157,277	1.727	0.34
363,747	1.992	0.00	281,655	1.827	0.00	371,705	1.733	0.00
Square obstacle			Rhomboid obstacle					
No. of elements	\overline{Nu}	% error	No. of elements	\overline{Nu}	% error			
28,011	1.663	3.72	27,989	1.823	3.92			
66,832	1.705	1.30	66,754	1.871	1.39			
158,187	1.727	0.04	157,705	1.896	0.07			
289,061	1.727	0.00	288,435	1.897	0.00			

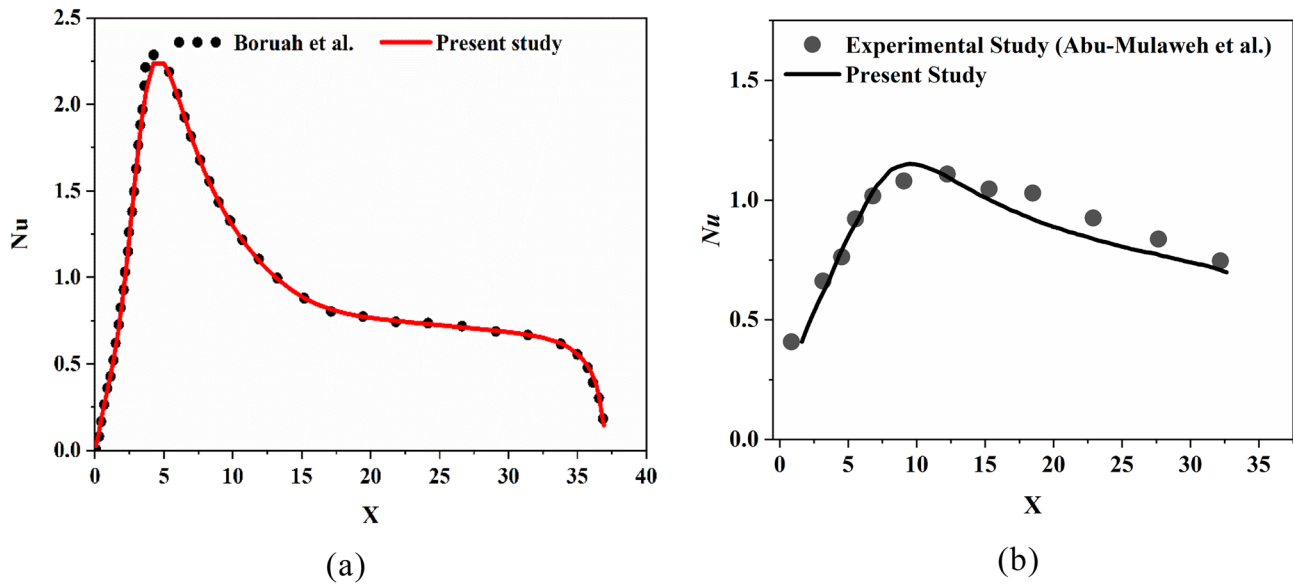


Fig. 2 Model validation: Nusselt number comparison with (a) Boruah et al. and (b) Abu-Mulaweh et al.

5.1.1 Flow and Temperature Fields

Streamline flow and temperature fields are important for understanding thermohydraulic transport characteristics in a BFSC. Hence, the streamlined distribution and velocity magnitude for five different obstacle shapes is shown in Fig. 3, and for Ri is 1 and Re is 100.

Figure 3 shows the recirculation zone near the backward-facing step along the bottom wall. The insertion of obstacle geometry significantly reduces the length of the recirculation zone near the step. The number of smaller recirculation zones is observed with decreasing length as the flow proceeds downstream. However, the size and vorticity of the recirculation zone are greatest in the case of rhomboid obstacles. The rhomboid geometry has higher symmetric geometry along the axis of flow, which leads to a maximum Nusselt number in the case of flow over the rhomboid obstacle (refer to Fig. 5). On the contrary, the size and number of recirculation zones formed is lowest in the case of the elliptical obstacle. Because a strong vorticity field is generated at the downstream side of these geometries, the vorticity field compresses the streamlines up to the local peak of the sinusoidal wall, which develops a weakened vortex near the heated wall.

The isotherms are plotted in Fig. 4 for different obstacle geometries in BFSC at $Ri = 1$ and $Re = 100$. It can be observed from Fig. 4a that the bottom heated wall has a dense magnitude of contours at pre-expansion length (L_1), as described in the literature (Feng et al. 2023). The insertion of obstacles generates a much denser contour near the upstream sides of obstacles, resulting in high heat transfer in that region (refer to Fig. 5). The combined contours of 0.7

and 0.5 revealed different contoured areas in different cases, depending on the obstacle sizes. The area mentioned above is greater in the case of triangular and rhomboid geometry, which can be attributed to the fact that these geometries have minimum cross-sectional area for the flow of fluids. The variation of contour lines in the case of an elliptical obstacle is very minimal because the elliptical profile has the lowest fluid resistance.

5.1.2 Hydrothermal Characteristics

The local Nusselt number (Nu) with respect to the sinusoidal channel is plotted in Fig. 5 for different obstacle configurations. Figure 5 depicts the model variation of Nu with axial direction ($0 \leq X \leq 40$) of the channel for $Ri = 1$ and $Re = 100$. It can be observed from Fig. 5 that the insertion of obstacles generates local maxima in Nu before the obstacle location and depressed Nu lines after the obstacle location. It can be seen that an abrupt change in the cross-sectional area causes higher inertial dominance, as also observed in Fig. 3. It can also be noted that the variation among different obstacle configurations is significant to a channel length of 15. After that, a similarity in curves is observed among various obstacle configurations, which can be explained by the fact that an obstacle's insertion created a difference in plots for distinct obstacle configurations. However, when the initial impact of the obstacle diminishes, all flows find similarities in the flowing conditions and reach a steady curve for different obstacles. It can also be observed from Fig. 5 that rhomboid and triangular geometries generate the highest local maxima among different cases. Therefore, rhomboid and triangular geometry have far better local heat transfer.

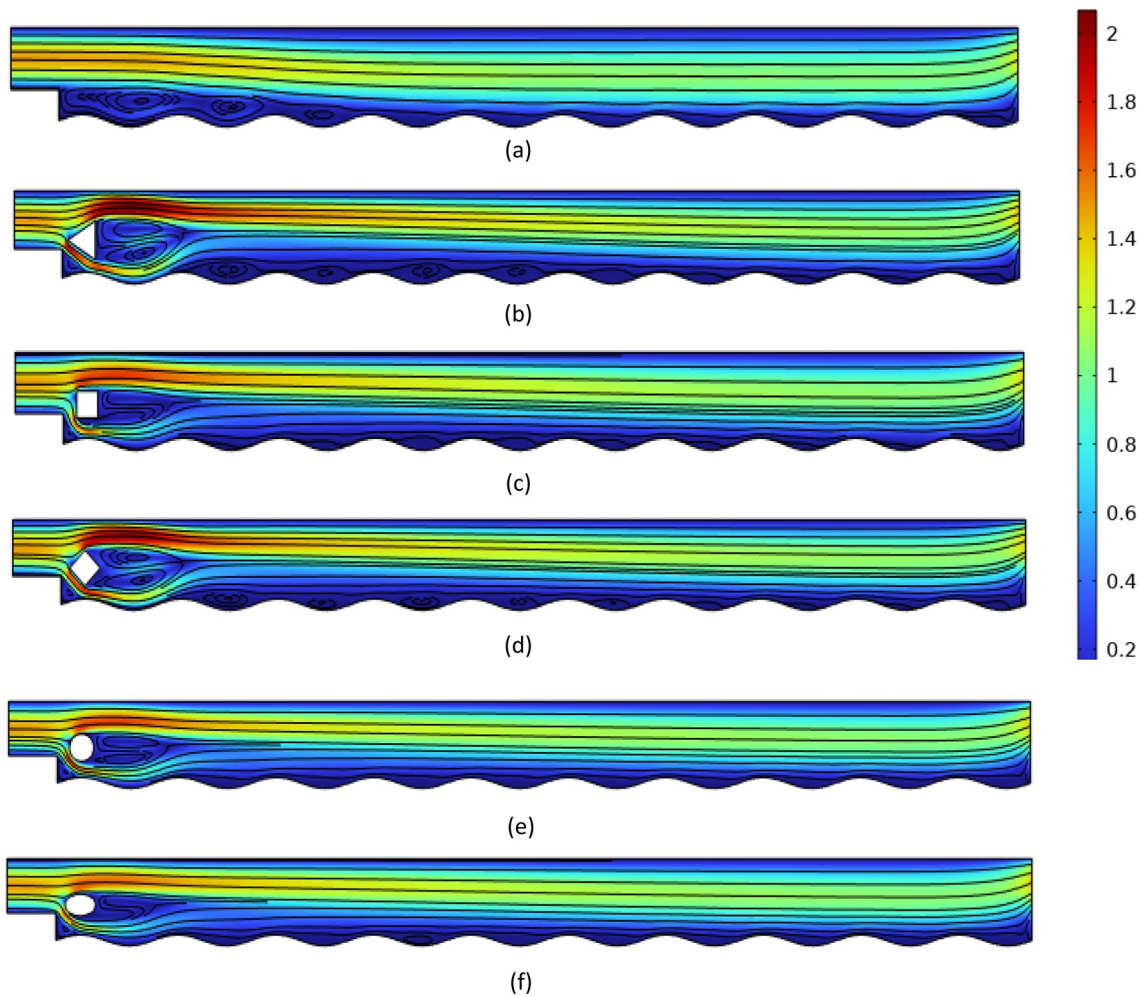


Fig. 3 Distribution of streamlines and velocity magnitude for the sinusoidal channel with different obstacle profiles: (a) without obstacle, (b) triangular obstacle, (c) square obstacle, (d) rhomboid obstacle, (e) circular obstacle, and (f) elliptical obstacle at $Ri = 1$ and $Re = 100$

Figure 6a is plotted for different obstacle configurations for the average Nusselt number (\overline{Nu}) with variation in Ri . It can be noted from Fig. 6a that the value of \overline{Nu} is found to be higher for all obstacle configurations than the reference case which can be explained by the fact that Nu in the upstream region for BFSC with an obstacle is significantly higher than the channel without an obstacle. Figure 6a shows that the triangular obstacle has maximum \overline{Nu} for most of Ri . This is because triangular configurations have the lowest side number for the equal area that is in direct contact with the fluid. Hence, most triangular circumferences are in contact with fluid flow.

The literature establishes that higher pumping power makes heat transfer increase possible (Boruah et al. 2018). The pressure drop (ΔP) for different obstacle cases with further Ri are plotted in Fig. 6b. It can be seen in Fig. 6b that the incorporation of obstacle geometries in BFSC generates a higher pressure drop irrespective of the type of obstacle

geometry as compared to BFSC without obstacles. It can be seen that the insertion of an obstacle causes recirculation, which is a key parameter in generating higher irreversibility. It is also seen that as ΔP increases with an increase in Ri irrespective of obstacle shapes and configurations. Figure 6b also shows that the pressure difference for triangular obstacle configurations is the highest, as it generates the highest fluid resistance.

5.1.3 Irreversibility

System irreversibility is presented as entropy generation, which dictates design performance. Thus, an efficient designer must clearly understand irreversibility and its different types (Boruah et al. 2018); therefore, two types of irreversibility are studied in the present investigation. The different obstacle geometries are presented for system irreversibility due to heat transfer (N_{Thermal}), system irreversibility due to viscous dissipation (N_{Viscous}), and total

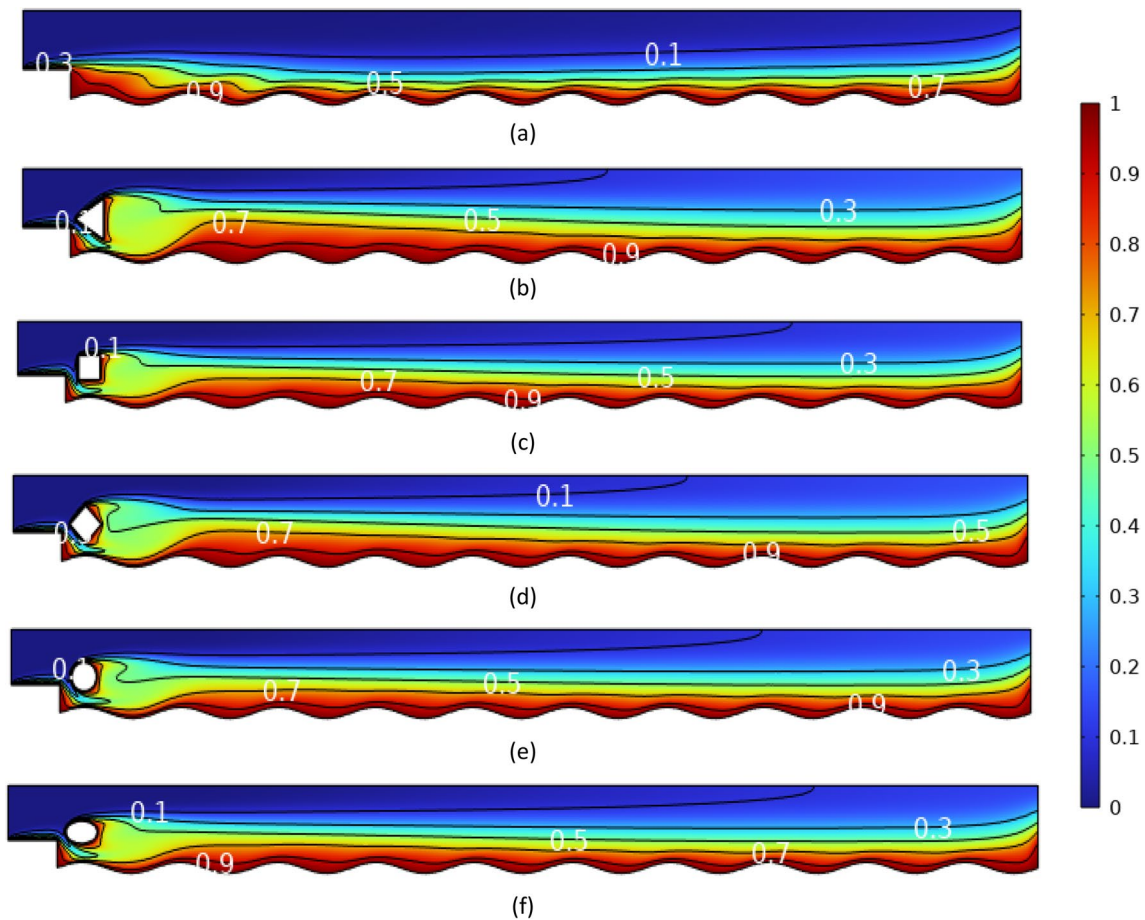


Fig. 4 Isotherm contours for the sinusoidal channel with different obstacle profiles: (a) without obstacle, (b) triangular obstacle, (c) square obstacle, (d) rhomboid obstacle, (e) circular obstacle, and (f) elliptical obstacle at $Ri = 1$ and $Re = 100$

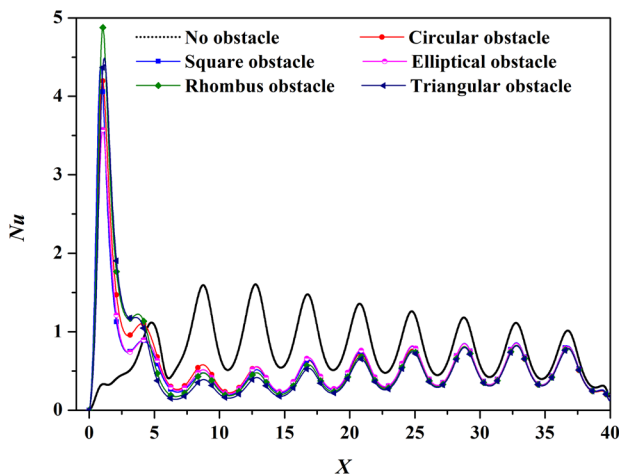


Fig. 5 Nusselt number variation for obstacle configurations with respect to the sinusoidal channel at $Ri = 1$ and $Re = 100$

irreversibility N_{Total} in Fig. 7, respectively, for different Ri . It can also be observed that the triangular geometries share the highest irreversibility of all investigated cases, which can be explained by the triangular case having the highest difference in obstacle cross-sectional areas in the flow direction. It can also be observed that the irreversibility generated for all obstacle cases has higher values than without obstacle cases. An increase in Ri leads to an increase in temperature and velocity gradient, collectively affecting the increase in $N_{Thermal}$ and $N_{Viscous}$, respectively.

Figure 8 depicts the variation of the Bejan number (Be) for $Ri = 1$ and $Re = 100$ for the entire channel length ($0 \leq X \leq 40$). Figure 8 shows that the variation of different obstacles for Be plots is insignificant after a channel length of 20, which can be attributed to the fact that flow exhibits similar geometries for post-obstacle length. The variation among lines reached the highest difference in obstacle locations due to the higher inertial dominance near the obstacle region. After the obstacle location, the variation started to diminish, and at 40, the variation reached its minimum level. Local minima for Be downstream of the channel for all the

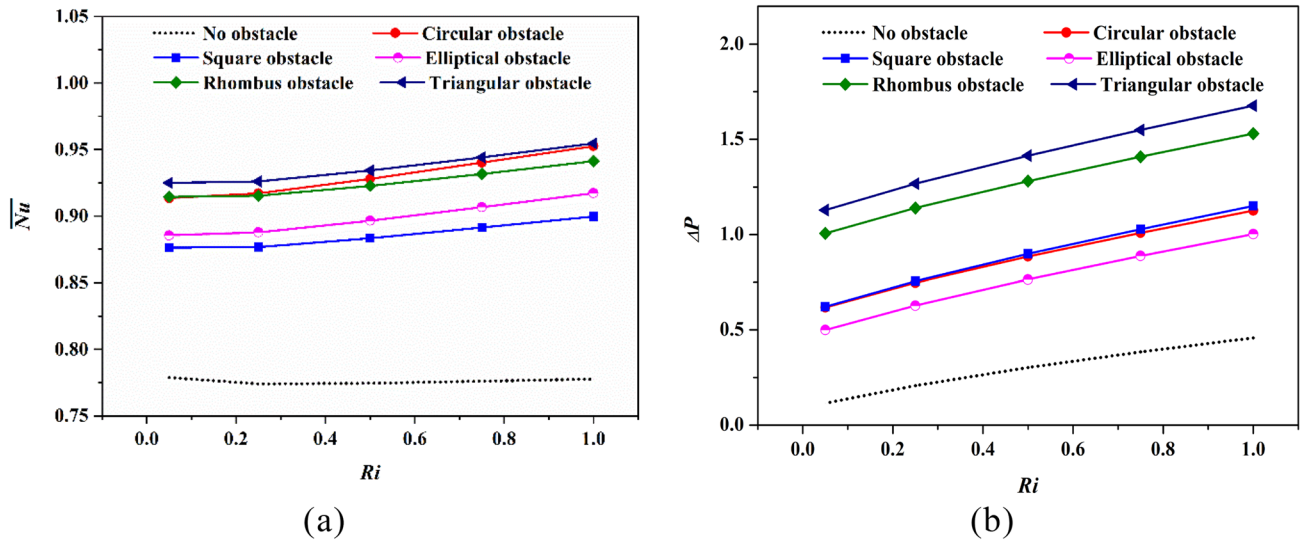


Fig. 6 Effect of Ri on \overline{Nu} , ΔP for obstacle configurations at $Re = 100$

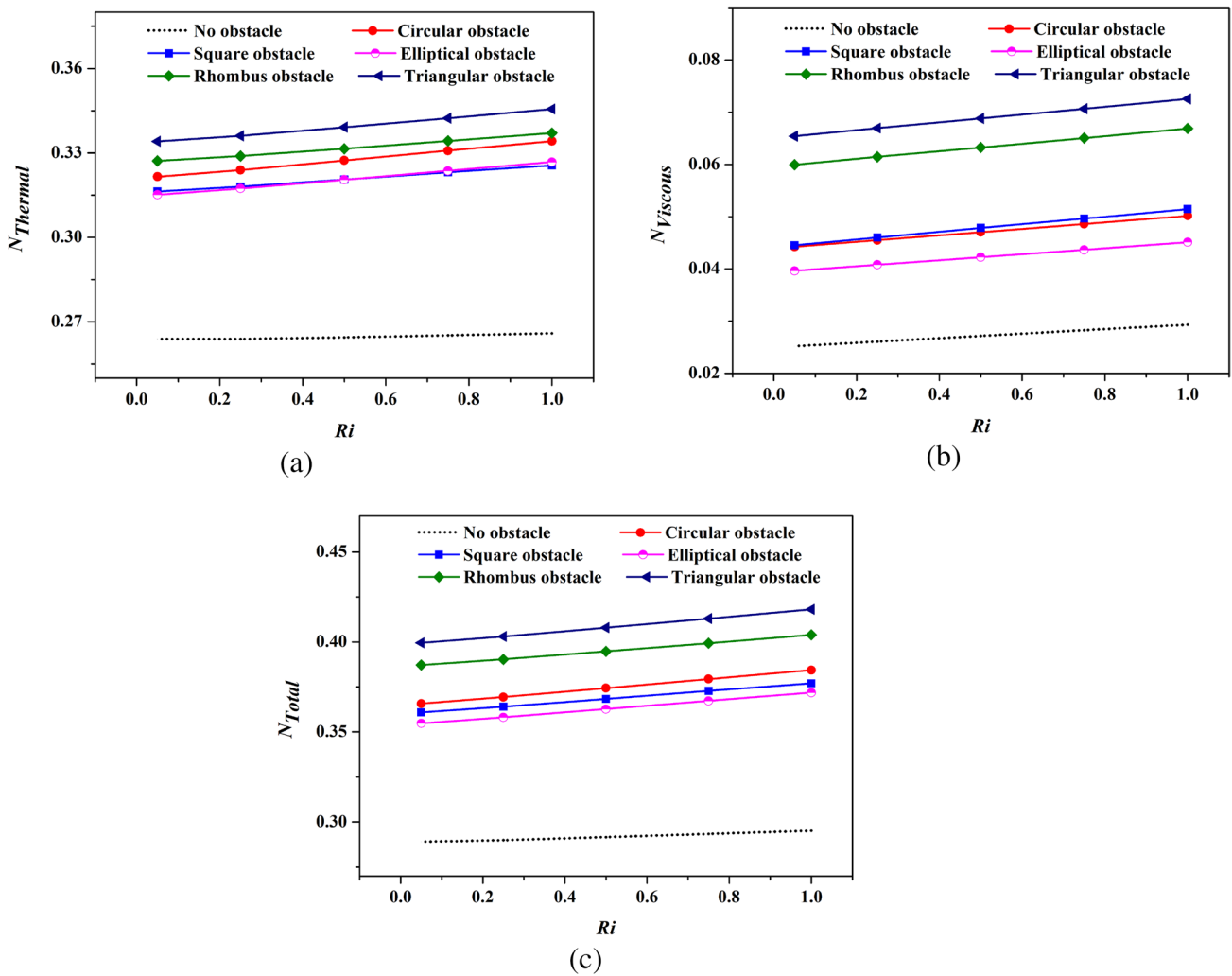


Fig. 7 Variation of $N_{Thermal}$, $N_{Viscous}$, N_{Total} for different Ri at $Re = 100$

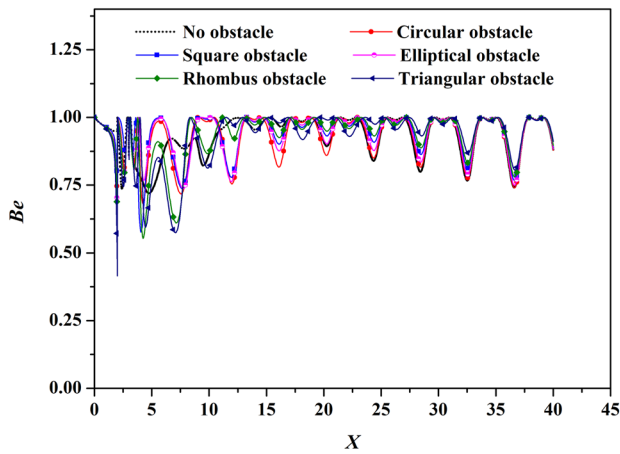


Fig. 8 Bejan number variation for sinusoidal BFSC wall at $Ri=1$ and $Re=100$

obstacle configurations is the same as without an obstacle. Figure 8 also depicts that triangular and rhomboid obstacles share the highest variation in the obstacle region, which can

be noted as N_{Total} . These outperformed the other cases presented in Fig. 7c.

The Be contours for different obstacle geometries are illustrated in Fig. 9. The insertion of obstacles shifts denser contour lines near the adiabatic wall, as shown in Fig. 9. Because of the insertion of obstacles reducing the cross-sectional area for flow generating inertial dominance near the obstacle region. The bottom wall and obstacle are kept at a higher temperature. The adiabatic upper wall causes lower magnitude contours due to a lower temperature gradient. The peak value of the local Nusselt number was maximum for the BFSC with a rhomboid obstacle (refer to Fig. 5). It has been observed that both pressure drop and total irreversibility increase with the increase in Ri irrespective of the shape of the obstacle and are found to be maximum in the case of a triangular obstacle (refer to Figs. 6 and 7).

5.1.4 Selection of the Optimal Obstacle Geometry

The selection of optimal obstacle geometry is essential for conducting an in-depth investigation of obstacle location

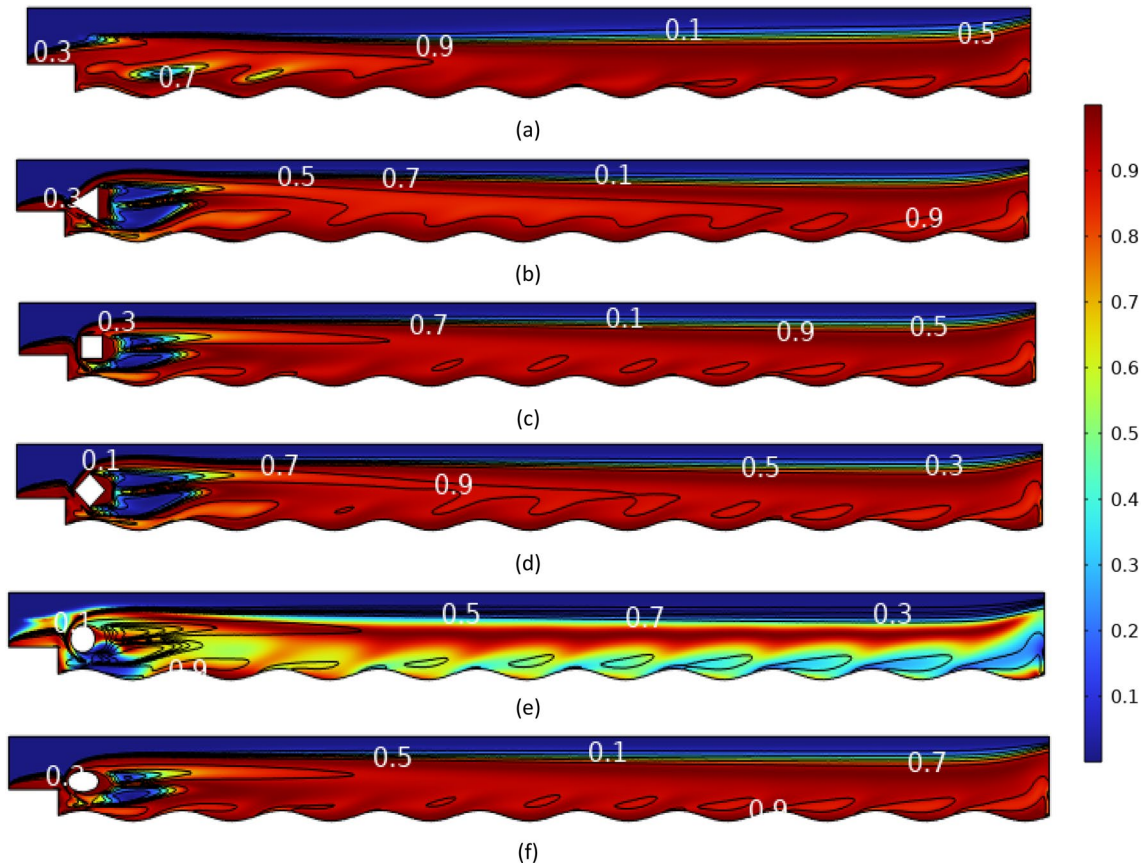


Fig. 9 Bejan number contours for BFSC with different obstacle configurations: **a** without obstacle, **b** triangular obstacle, **c** square obstacle, **d** rhomboid obstacle, **e** circular obstacle, and **f** elliptical obstacle at $Ri=1$ and $Re=100$

and orientation study. Hence, a hydrothermal factor is introduced, i.e., the ratio of the Nusselt number to pressure difference, as shown in Fig. 10. It can be noted that an elliptical obstacle has the highest hydrothermal factor. Although the elliptical configuration has a moderate Nusselt number, its corresponding pressure difference is so low with an increase in Richardson number that it leads to the highest hydrothermal factor. Hence, elliptical obstacle configurations are further analyzed for obstacle location and orientation analysis.

5.2 Effect of Elliptical Obstacle Location

After establishing that the elliptical obstacle is optimal with hydrothermal and irreversibility characteristics, the influence of an obstacle to step obstruction distances (L_x and L_y) on the hydrothermal and irreversibility are analyzed, obstacles are placed at different L_x , namely, 1, 5, 10, 20, 30, and 39 and L_y , namely, 0.7, 1.0, 1.3, 1.6, 2.2, and 2.5. An optimum elliptical obstacle location with favorable characteristics is expected. The analysis is presented in the following sections.

5.2.1 Hydrothermal Characteristics

The effect of an obstacle-to-step obstruction distances (L_x and L_y) is studied for hydrothermal performance is shown in Fig. 11 for $Ri=0.5$ and $Re=100$. The different locations for the study are $L_x=1, 5, 10, 20, 30$, and 39 , whereas L_y is presented on the y-axis. It is clear from Fig. 11a that as L_y increases, the magnitude of Nu gradually increases up to $L_y=2$ and then decreases, except for the case of $L_x=1$. This means that the increase in obstacle to step distance along the y-axis compresses the fluid to pass by the hot bottom wall,

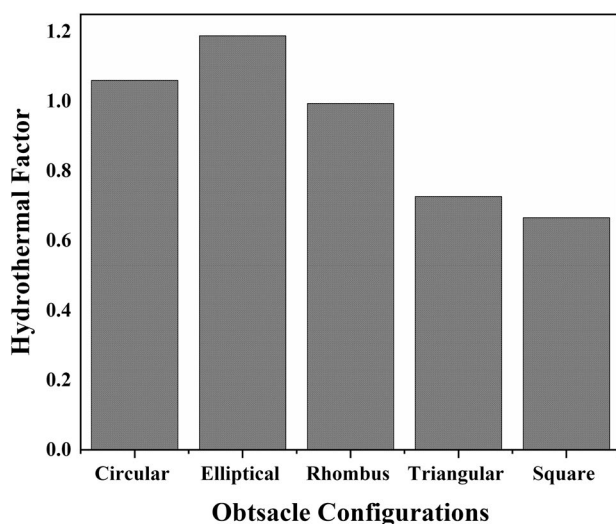


Fig. 10 Hydrothermal factor for different obstacle shape configurations

and the recirculation length also decreases for these cases. Moreover, as L_x increases, the Nu value linearly increases. This means that at lower L_x and L_y combinations, the effect of BFS is insignificant, and with the development of recirculation zones, the heat transfer increases for higher L_x and L_y combinations.

Figure 11b illustrates the effect of an obstacle-to-step obstruction distances (L_x and L_y) at $Ri=0.5$ and $Re=100$ on pressure drop. It can be noted that $L_x=1$ has the highest pressure drop for $L_y=1.9$. It can be depicted from the fact that $L_x=1$ for 1st two locations of L_y (0.7 and 1) received the flow after BFS, and no direct flow is obtained. However, L_y (1.3 and above locations) receives direct flow and is first obstructed by its front part.

5.2.2 Irreversibility Characteristics

Figure 11c illustrates the influence of obstacle-to-step distances on irreversibility performance. Figure 11c shows that N_{Total} increases with an increase in L_y to step distance. It is expected as an increase in L_y leads to an increase in thermal and frictional irreversibility.

It can also be observed that except when $L_x=1$, all plots share the same pattern, with some deviation. This can be explained by the fact that $L_x=1$ is the closest to BFS, with the greatest impact; however, the flow of other configurations is influenced by their geometry.

5.2.3 Selection of the Optimal Location for an Elliptical Obstacle

The selection of the optimal location for elliptical obstacle configurations is essential for conducting an in-depth investigation for angular orientation study. Hence, a hydrothermal factor is investigated for different L_x and L_y locations of elliptical obstacle configurations as illustrated in Fig. 12. It can be noted that the highest hydrothermal factor is achieved for L_y greater than 2, and an L_x range between 10 and 20. Hence, elliptical obstacle configurations with locations ($L_x=10$ and $L_y=2.2$), ($L_x=20$ and $L_y=2.2$) are further analyzed for orientation analysis.

5.3 Effect of Angle of Elliptical Obstacle

After establishing that elliptical obstacles with locations ($L_x=10$ and $L_y=2.2$), ($L_x=20$ and $L_y=2.2$) are considered optimal geometry and location, the effect of obstacle inclination angle (θ_b), i.e., the orientation angle of the obstacle from the x-axis on the hydrothermal and irreversibility characteristics, is analyzed. Obstacles are varied for different orientations of θ_b including $0^\circ, 30^\circ, 60^\circ, 90^\circ, 120^\circ$, and 150° . It is expected that an optimum inclination for the

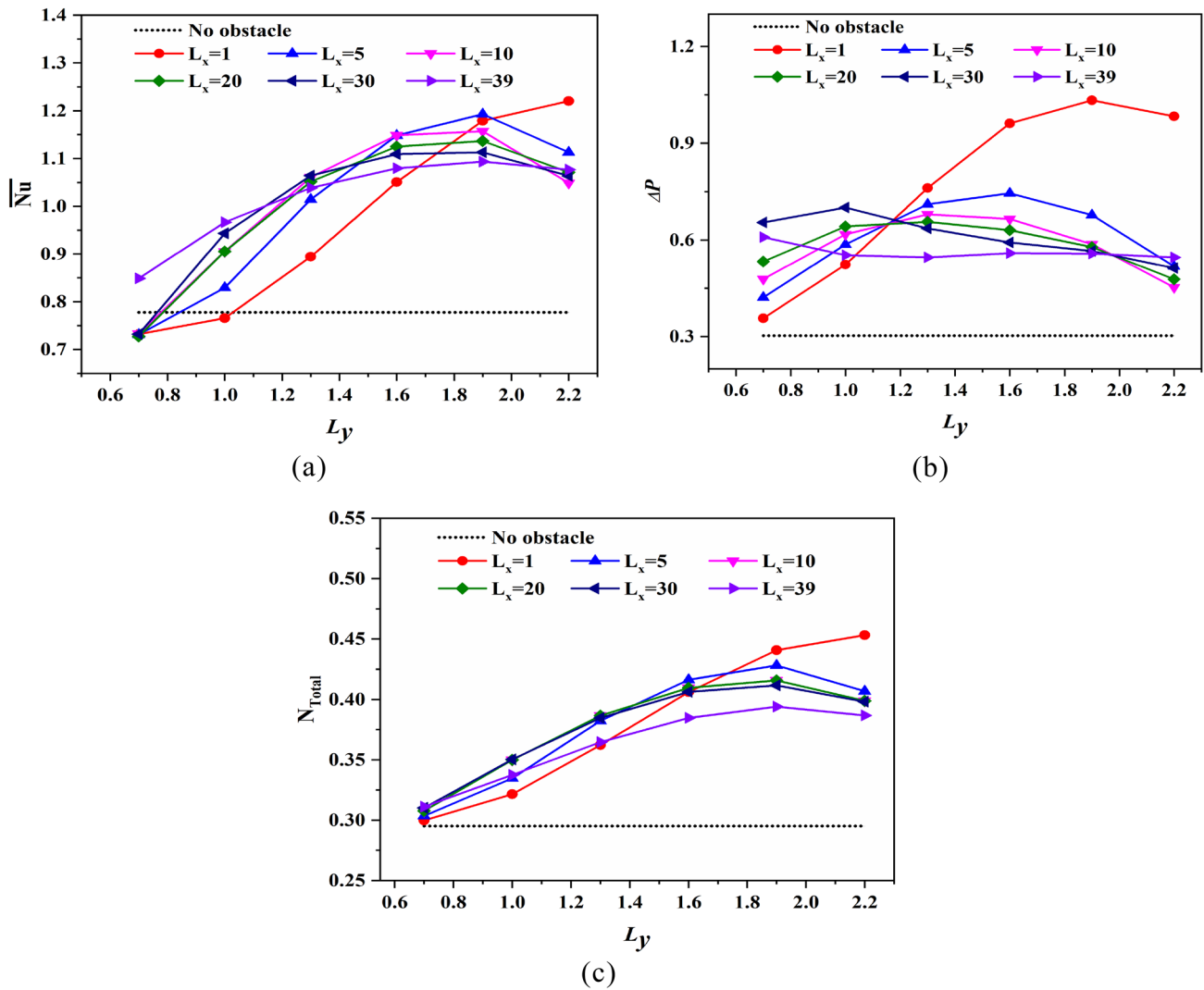


Fig. 11 Influence of the obstacle to step distance (L_x) on \overline{Nu} , ΔP and N_{Total} at $Ri=0.5$ and $Re=100$

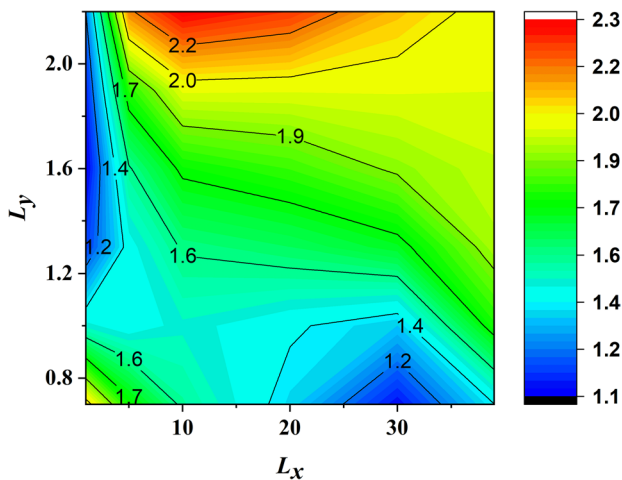


Fig. 12 Hydrothermal factor for different elliptical obstacle locations

best-performing location cases of elliptical obstacles with favorable characteristics will be found. The analysis is presented in the following sections.

5.3.1 Hydrothermal Characteristics

The hydrothermal characteristics illustrating the average Nusselt number (\overline{Nu}), pressure drop (ΔP) with an angle of obstacles for both optimum cases of elliptical obstacle ($L_x = 10$ and $L_y = 2.2$), ($L_x = 20$ and $L_y = 2.2$) are shown in Fig. 13 at $Ri=0.5$ and $Re=100$. Figure 13(a) illustrates the effect of angles of obstacles on \overline{Nu} . It can be observed that obstacle orientation significantly affects \overline{Nu} . Moreover, a cyclic performance is found as \overline{Nu} increases when obstacle orientation is varied from 0° to 90° and \overline{Nu} decreases when obstacle orientation varies from 90° to 150° . As the angle increases to 90° , the fluid inertial force is primarily diverted

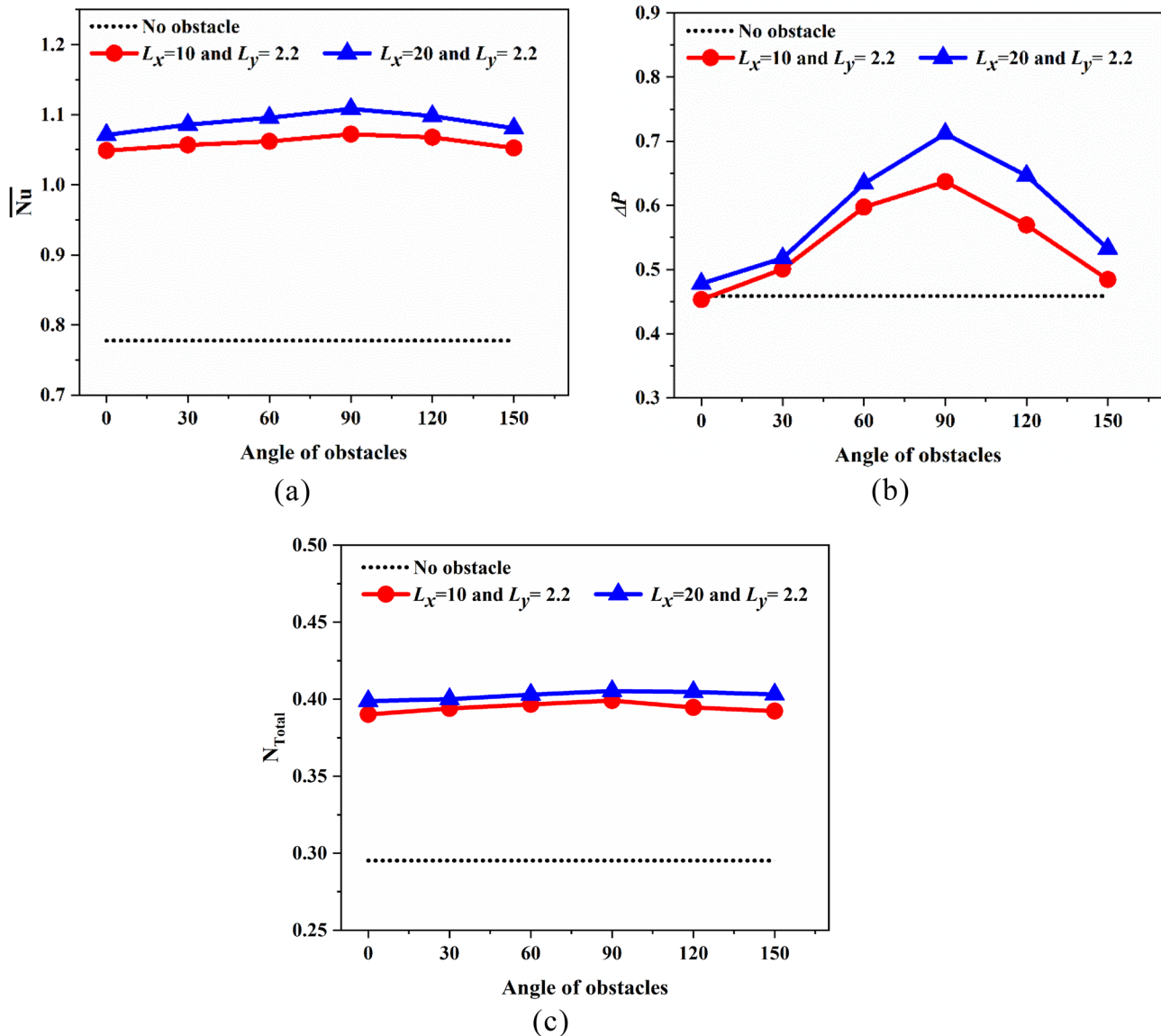


Fig. 13 Effect of an obstacle to obstacle inclination (θ_b) on \overline{Nu} , ΔP and N_{Total} at $Ri=0.5$ and $Re=100$

to the sinusoidal BFSC wall and improves heat transfer. The later decrease can be justified because as the angle increases from 90°, the fluid generates larger recirculation zones near the step. The obstacle-oriented direction of fluid inertial force also decreases towards the sinusoidal BFSC wall. It can also be observed that the optimum case ($L_x=20$ and $L_y=2.2$) results in higher Nu . It can be depicted that the optimum case ($L_x=20$ and $L_y=2.2$) directs the fluid inertia to reach the sinusoidal BFSC wall after a considerable distance from the BFSC step, and thus generates a higher Nu .

It is revealed from Fig. 13b that variation in pressure drop also follows the same trend (up to 90°, the pressure drop increases and then decreases) because angular orientation varies inertial dominance in a cyclic manner. Figure 13b also

shows that ($L_x=10$ and $L_y=2.2$) have lower pressure drop than ($L_x=20$ and $L_y=2.2$), which is because ($L_x=10$ and $L_y=2.2$) have geometrical proximity to the BFSC step and obstacle introduction near ($L_x=20$) directs fluid inertia to move quickly to the sinusoidal BFSC channel.

5.3.2 Irreversibility Characteristics

Figure 13c illustrates the influence of different orientations of obstacles on the total irreversibility at $Ri=0.5$ and $Re=100$. It is observed from Fig. 13c that both cases have higher values than the reference cases, as before, and also have the same pattern of increase and decrease of about 90°,

which is because viscous entropy generation follows the orientation cyclically.

5.3.3 Selection of the Optimal Orientation for Elliptical Obstacle Configuration

The selection of the optimal orientation for elliptical obstacle configurations is essential to conclude the results. Hence, a hydrothermal factor is investigated for different orientations (θ_b) of elliptical obstacle configurations, as illustrated in Fig. 14. The highest hydrothermal factor is achieved for angular orientation ($\theta_b = 0^\circ$). It is expected as the lowest pressure drop is recorded for this orientation (refer to Fig. 13b). Hence, elliptical obstacle configurations with locations ($L_x = 10$ and $L_y = 2.2$), ($L_x = 20$ and $L_y = 2.2$) have the optimal orientation as ($\theta_b = 0^\circ$).

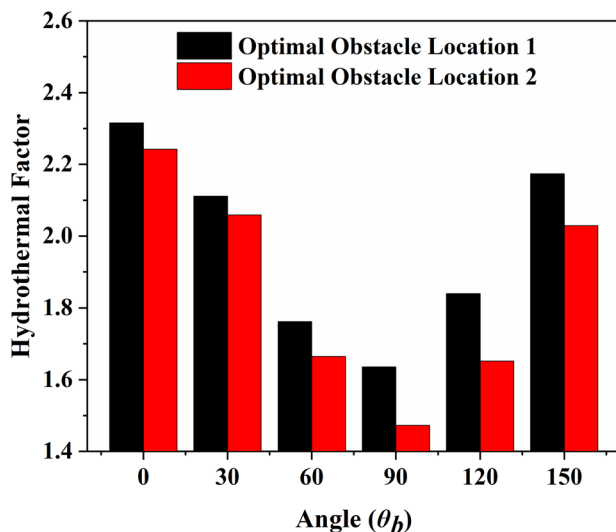


Fig. 14 Hydrothermal factor for two elliptical obstacle orientations for optimal locations

5.4 Comparison of Optimum System with the Reference Case

The interplay of obstacle geometry, obstacle angle, and obstacle-to-step obstruction distances is investigated, and recommends an optimum system consisting of best-performing obstacle geometry, best-performing obstacle angle, and best-performing location as per hydrothermal factor is compared with the reference case (no obstacle configuration). The two optimum systems considered for the present study are elliptical obstacles with an inclination angle of 0° . The obstacle location ($L_x = 10$ and $L_y = 2.2$), ($L_x = 20$ and $L_y = 2.2$) is compared with the no-obstacle reference case. The analysis is presented in the next section.

5.4.1 Hydrothermal Characteristics

Figure 15 shows the streamlines and velocity distributions for two optimum cases with the best obstacle geometry, best-performing obstacle angle, and best-performing location. It can be noted that the introduction of an elliptical obstacle at ($L_x = 10$ and $L_y = 2.2$) reduced the primary recirculation zone after the backward-facing step channel, which reduces heat transfer. Figure 16a illustrates the comparison between optimum and reference cases for \overline{Nu} across Ri . It is worth mentioning that both optimum systems have a greater magnitude of \overline{Nu} as compared to the reference case. It can be attributed to the fact that changing locations and orientation of obstacles generate favorable transport and heat transfer characteristics by placement and size of recirculation zones and reattachment length. The optimum system 1 has a lower Nu value at low Ri ; as Ri increases, there is a comparatively higher increase than system 2.

Both optimum systems of obstacles on pressure drop characteristics are illustrated in Fig. 16b for $Re = 100$. Figure 16b shows that ΔP increases with an increase in Ri for both cases. It can also be observed that optimum system 2 has a higher pressure drop than case 1. It can be seen that case 1 has geometrical proximity with inflow and causes

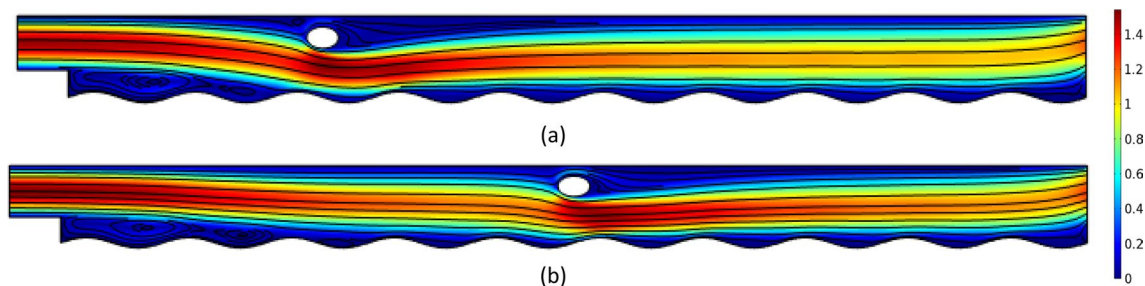


Fig. 15 Distribution of streamlines and velocity magnitude for the sinusoidal channel with different obstacle profiles: **a** elliptical obstacle at $L_x = 10$, $L_y = 2.2$, and **b** elliptical obstacle at $L_x = 20$, $L_y = 2.2$ at $Ri = 0.5$ and $Re = 100$

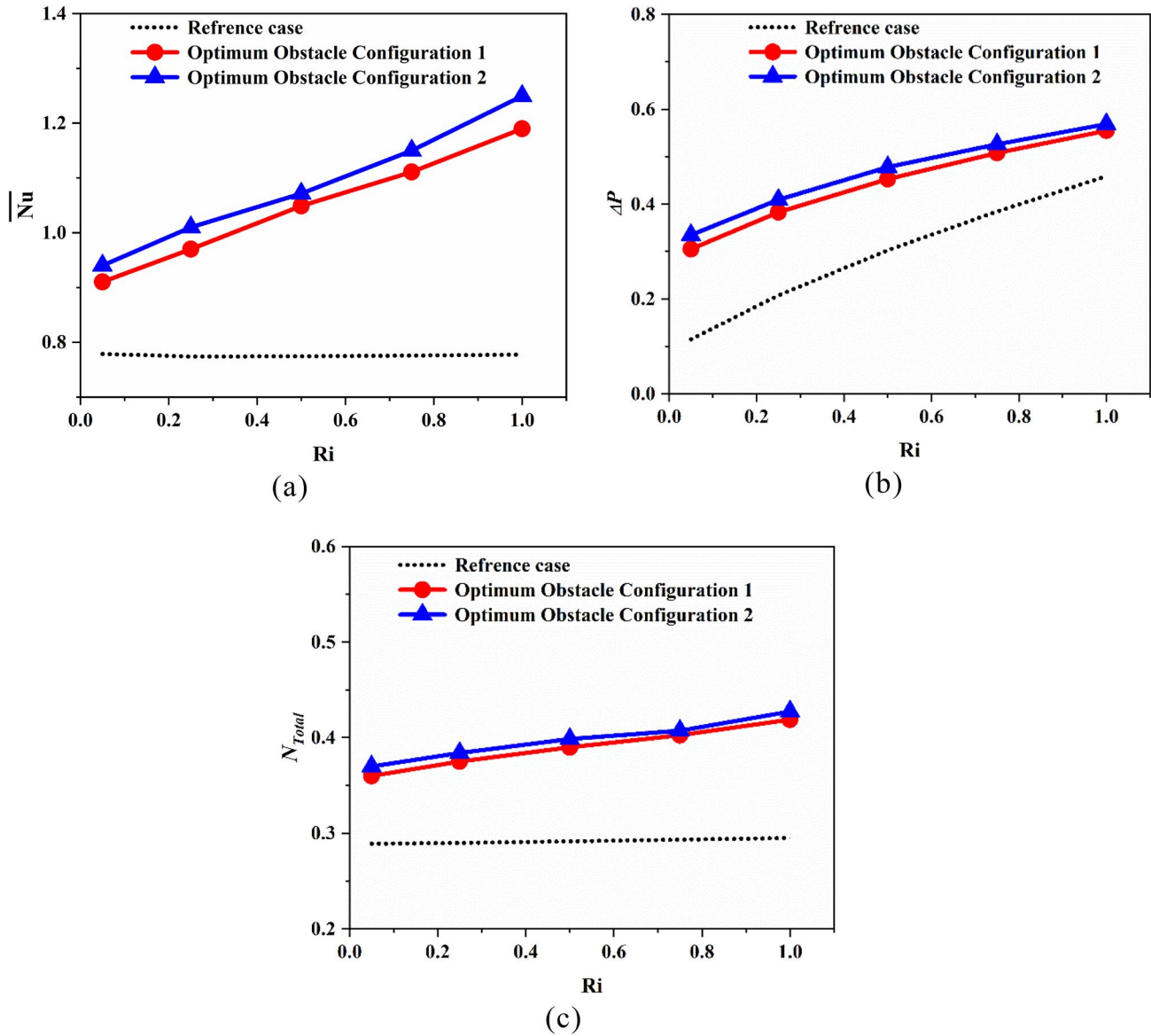


Fig. 16 Comparison of two optimum cases with reference case on **a** \overline{Nu} , **b** ΔP and **c** N_{Total} at $Re = 100$

a significant reduction in the recirculation zone along the sinusoidal BFSC channel.

5.4.2 Irreversibility Characteristics

The total irreversibility obtained in BFSC due to two obstacles containing optimum systems is plotted in Fig. 16c along with the reference case without obstacle. It can be observed that both systems have significantly higher irreversibility in comparison to the reference case, which can be explained by the fact that there is a cross-section reduction with the insertion of an obstacle.

This generates inertial dominance causing irreversibility due to thermal and overall contributed to N_{Total} . The average assessment shows that optimum systems 1 and 2 has 34.95% and 36.15% higher average Nusselt number (\overline{Nu}) value, 33.44% and 35.29% higher irreversibility (N_{Total}), 70.49% and 81.47% higher pressure drop (ΔP), respectively, when compared to without obstacle reference case.

6 Conclusions

The present investigation discusses two-dimensional, steady, laminar, incompressible, and mixed convective flow and highlights the impact of obstacle configuration on thermo-hydraulic and irreversibility characteristics for a sinusoidal backward-facing step channel. In this context, the interplay of the obstacle configurations, namely profile, step obstruction distance (L_x and L_y), and obstacle orientations, are studied. Some of the noble conclusions extracted from the present investigation are pointed out below.

- The length of the reattachment region decreases with obstacle inclusion, irrespective of the investigated profile. Square obstacle configuration generates the shortest reattachment among different obstacle geometries.
- The local Nusselt number is greatest at the obstacle location irrespective of the cases. Moreover, the value of the local Nusselt number is the greatest for the rhomboid obstacle.
- Total irreversibility increases with the increase in the Richardson number and is found to be greatest for the triangular obstacles.
- Elliptical obstacle configuration is found to be optimal, with higher heat transfer, lower pressure drop, and total irreversibility.
- The best-performing combination for making optimum cases was considering an elliptical obstacle with an orientation of 0° and having locations of ($L_x = 10$ and $L_y = 2.2$), ($L_x = 20$ and $L_y = 2.2$).
- The average assessment shows that optimum systems 1 and 2 have 34.95% and 36.15% higher average Nusselt number (\overline{Nu}) values, 33.44% and 35.29% higher irreversibility (N_{Total}), and 70.49% and 81.47% higher pressure drop (ΔP), respectively, when compared to the reference case without obstacle

References

Abu-Mulaweh HI, Armaly BF, Chen TS (1993) Measurements of laminar mixed convection in boundary-layer flow over horizontal and inclined backward-facing steps. *Int J Heat Mass Transf* 36:1883–1895. [https://doi.org/10.1016/S0017-9310\(05\)80176-0](https://doi.org/10.1016/S0017-9310(05)80176-0)

Abu-Mulaweh HI, Armaly BF, Chen TS (1995) Laminar natural convection flow over a vertical backward-facing step. *J Heat Transfer* 117:895–901. <https://doi.org/10.1115/1.2836308>

Abu-Nada E (2006) Entropy generation due to heat and fluid flow in backward facing step flow with various expansion ratios. *Int J Exergy* 3:419–435. <https://doi.org/10.1504/IJEX.2006.010234>

Al-aswadi AA, Mohammed HA, Shuaib NH, Campo A (2010) Laminar forced convection flow over a backward facing step using nanofluids. *Int Commun Heat Mass Transf* 37:950–957. <https://doi.org/10.1016/J.ICHEATMASSTRANSFER.2010.06.007>

Ali MR, Al-Khaled K, Hussain M et al (2022) Effect of design parameters on passive control of heat transfer enhancement phenomenon in heat exchangers—a brief review. *Case Stud Therm Eng*. <https://doi.org/10.1016/J.CSITE.2022.102674>

Anyanwu IS, Hou Y, Xi F et al (2019) Comparative analysis of two-phase flow in sinusoidal channel of different geometric configurations with application to PEMFC. *Int J Hydrogen Energy* 44:13807–13819. <https://doi.org/10.1016/J.IJHYDENE.2019.03.213>

Avancha RVR, Pletcher RH (2002) Large eddy simulation of the turbulent flow past a backward-facing step with heat transfer and property variations. *Int J Heat Fluid Flow* 23:601–614. [https://doi.org/10.1016/S0142-727X\(02\)00156-X](https://doi.org/10.1016/S0142-727X(02)00156-X)

Bahiraei M, Gharagozloo K, Alighardashi M, Mazaheri N (2017) CFD simulation of irreversibilities for laminar flow of a power-law nanofluid within a minichannel with chaotic perturbations: an innovative energy-efficient approach. *Energy Convers Manag* 144:374–387. <https://doi.org/10.1016/J.ENCONMAN.2017.04.068>

Barbosa Saldana JG, Anand NK, Sarin V (2005) Numerical simulation of mixed convective flow over a three-dimensional horizontal backward facing step. *J Heat Transfer* 127:1027–1036. <https://doi.org/10.1115/1.2005272>

Barton IE (1998) The entrance effect of laminar flow over a backward-facing step geometry. *Int J Numer Methods Fluids* 25:633–644. [https://doi.org/10.1002/\(SICI\)1097-0363\(19970930\)25:6%3c633::AID-FLD551%3e3.0.CO;2-H](https://doi.org/10.1002/(SICI)1097-0363(19970930)25:6%3c633::AID-FLD551%3e3.0.CO;2-H)

Baytas AC, Pop I (1999) Free convection in oblique enclosures filled with a porous medium. *Int J Heat Mass Transf* 42:1047–1057. [https://doi.org/10.1016/S0017-9310\(98\)00208-7](https://doi.org/10.1016/S0017-9310(98)00208-7)

Beigzadeh R, Ozairy R (2019) Developing predictive models for analysis the heat transfer in sinusoidal wavy channels. *Therm Sci Eng Prog* 14:100425. <https://doi.org/10.1016/J.TSEP.2019.100425>

Bejan A (1998) Entropy generation minimization: the new thermodynamics of finite-size devices and finite-time processes. *J Appl Phys* 79:1191. <https://doi.org/10.1063/1.362674>

Bekhradinasab A, Al-Zaili J, Vakili-pour S (2021) Large eddy simulation of separated flow to investigate heat transfer characteristics in an asymmetric diffuser subjected to constant wall heat flux. *Int Commun Heat Mass Transf* 128:105634. <https://doi.org/10.1016/J.ICHEATMASSTRANSFER.2021.105634>

Boruah MP, Randive PR, Pati S (2018) Hydrothermal performance and entropy generation analysis for mixed convective flows over a backward facing step channel with baffle. *Int J Heat Mass Transf* 125:525–542. <https://doi.org/10.1016/J.IJHEATMASSTRANSFER.2018.04.094>

Chamkha AJ, Selimefendigil F (2018) Forced convection of pulsating nanofluid flow over a backward facing step with various particle shapes. *Energies* 11:1–19. <https://doi.org/10.3390/en11113068>

Chang SW, Lees AW, Chou TC (2009) Heat transfer and pressure drop in furrowed channels with transverse and skewed sinusoidal wavy walls. *Int J Heat Mass Transf* 52:4592–4603. <https://doi.org/10.1016/j.ijheatmasstransfer.2009.02.039>

Feng G, Zhang J, Chen M et al (2023) Diffusion characteristics of liquid kerosene with heat transfer in a strut-equipped supersonic combustor. *Acta Astronaut* 203:246–251. <https://doi.org/10.1016/J.ACTAASTRO.2022.12.007>

Geng J, Zheng G, Wang H, Huang J (2023) Enhanced of fluids mixing and heat transfer in a novel SSK static mixer Organic Rankine Cycle direct contact heat exchanger. *Appl Therm Eng* 219:119580. <https://doi.org/10.1016/J.APPLTHERMALENG.2022.119580>

Ghasemi SE, Gouran S, Zolfagharian A (2021) Thermal and hydrodynamic analysis of a conducting nanofluid flow through a sinusoidal wavy channel. *Case Stud Therm Eng* 28:101642. <https://doi.org/10.1016/J.CSITE.2021.101642>



- Guo R, Heiselberg P, Hu Y et al (2021) Experimental investigation of convective heat transfer for night cooling with diffuse ceiling ventilation. *Build Environ* 193:107665. <https://doi.org/10.1016/J.BUILDENV.2021.107665>
- Heshmatian S, Bahiraei M (2017) Numerical investigation of entropy generation to predict irreversibilities in nanofluid flow within a microchannel: Effects of Brownian diffusion, shear rate and viscosity gradient. *Chem Eng Sci* 172:52–65. <https://doi.org/10.1016/J.CES.2017.06.024>
- Iwai H, Nakabe K, Suzuki K, Matsubara K (2000) The effects of duct inclination angle on laminar mixed convective flows over a backward-facing step. *Int J Heat Mass Transf* 43:473–485. [https://doi.org/10.1016/S0017-9310\(99\)00141-6](https://doi.org/10.1016/S0017-9310(99)00141-6)
- Jin W, Jia YX, Lei J et al (2022) Coupled heat transfer analysis of internal and film cooling of turbine blade under medium temperature conditions. *Appl Therm Eng* 214:118792. <https://doi.org/10.1016/J.APPLTHERMALENG.2022.118792>
- Kannan KG, Kamatchi R (2020) Augmented heat transfer by hybrid thermosyphon assisted thermal energy storage system for electronic cooling. *J Energy Storage* 27:101146. <https://doi.org/10.1016/J.EST.2019.101146>
- Khatoun B, Kumar Choudhary V, Kumar R et al (2022) Enhancement of heat transfer rate in shell & tube heat exchanger using CuO/Al₂O₃-water based nanofluids. *Mater Today Proc*. <https://doi.org/10.1016/J.MATPR.2022.10.258>
- Kolsi L, Selimefendigil F, Ben SL et al (2021) Forced convection of non-newtonian nanofluid flow over a backward facing step with simultaneous effects of using double rotating cylinders and inclined magnetic field. *Mathematics* 9:1–21. <https://doi.org/10.3390/math9233002>
- Korichi A, Oufar L (2007) Heat transfer enhancement in oscillatory flow in channel with periodically upper and lower walls mounted obstacles. *Int J Heat Fluid Flow* 28:1003–1012. <https://doi.org/10.1016/J.IJHEATFLUIDFLOW.2006.11.002>
- Kumar A, Kandasamy P, Chakraborty I, Hangshing L (2022) Analysis of energy consumption, heat and mass transfer, drying kinetics and effective moisture diffusivity during foam-mat drying of mango in a convective hot-air dryer. *Biosyst Eng* 219:85–102. <https://doi.org/10.1016/J.BIOSYSTEMSENG.2022.04.026>
- Lin JT, Armaly BF, Chen TS (1990) Mixed convection in buoyancy-assisting, vertical backward-facing step flows. *Int J Heat Mass Transf* 33:2121–2132. [https://doi.org/10.1016/0017-9310\(90\)90114-A](https://doi.org/10.1016/0017-9310(90)90114-A)
- Ma DD, Tang YX, Xia GD (2021) Experimental investigation of flow boiling performance in sinusoidal wavy microchannels with secondary channels. *Appl Therm Eng* 199:117502. <https://doi.org/10.1016/J.APPLTHERMALENG.2021.117502>
- Mahian O, Kianifar A, Kleinstreuer C et al (2013) A review of entropy generation in nanofluid flow. *Int J Heat Mass Transf* 65:514–532. <https://doi.org/10.1016/J.IJHEATMASSTRANSFER.2013.06.010>
- Mehrez Z, Bouterra M, El Cafi A et al (2009) The influence of the periodic disturbance on the local heat transfer in separated and reattached flow. *Heat Mass Transf Und Stoffuebertragung* 46:107–112. <https://doi.org/10.1007/S00231-009-0548-Z/FIGURES/8>
- Najafi Khaboshan H, Nazif HR (2019) Entropy generation analysis of convective turbulent flow in alternating elliptical axis tubes with different angles between pitches: a numerical investigation. *Heat Mass Transf Und Stoffuebertragung* 55:2857–2872. <https://doi.org/10.1007/S00231-019-02615-Z/FIGURES/17>
- Nie JH, Chen YT, Hsieh HT (2009) Effects of a baffle on separated convection flow adjacent to backward-facing step. *Int J Therm Sci* 48:618–625. <https://doi.org/10.1016/J.IJTHERMALSCI.2008.05.015>
- Nouri-Borujerdi A, Moazezi A (2018) Investigation of obstacle effect to improve conjugate heat transfer in backward facing step channel using fast simulation of incompressible flow. *Heat Mass Transf Und Stoffuebertragung* 54:135–150. <https://doi.org/10.1007/S00231-017-2086-4/TABLES/6>
- Oztop HF, Al-Salem K (2012) A review on entropy generation in natural and mixed convection heat transfer for energy systems. *Renew Sustain Energy Rev* 16:911–920. <https://doi.org/10.1016/J.RSER.2011.09.012>
- Selimefendigil F, Öztop HF, Chamkha AJ (2019) Mixed convection of pulsating ferrofluid flow over a backward-facing step. *Iran J Sci Technol-trans Mech Eng* 43:593–612. <https://doi.org/10.1007/s40997-018-0238-x>
- Selimefendigil F, Öztop HF (2016) Numerical study of forced convection of nanofluid flow over a backward facing step with a corrugated bottom wall in the presence of different shaped obstacles. 37: 1280–1292. <https://doi.org/10.1080/01457632.2015.1119617>
- Selimefendigil F, Öztop HF (2020) Hydro-thermal performance of CNT nanofluid in double backward facing step with rotating tube bundle under magnetic field. *Int J Mech Sci* 185:105876. <https://doi.org/10.1016/J.IJMECSCI.2020.105876>
- Shen W, Wang S (2022) Large eddy simulation of turbulent flow and heat transfer in a turbine disc cavity with impellers. *Int Commun Heat Mass Transf* 139:106463. <https://doi.org/10.1016/J.ICHEA.TMASSTRANSFER.2022.106463>
- Soong CY, Hsueh WC (1993) Mixed convection in a suddenly-expanded channel with effects of cold fluid injection. *Int J Heat Mass Transf* 36:1477–1484. [https://doi.org/10.1016/S0017-9310\(05\)80058-4](https://doi.org/10.1016/S0017-9310(05)80058-4)
- Taher A, Jones B, Fiorini P, Lagae L (2018) Analytical, numerical and experimental study on capillary flow in a microchannel traversing a backward facing step. *Int J Multiph Flow* 107:221–229. <https://doi.org/10.1016/j.ijmultiphaseflow.2018.06.018>
- Tropea CD, Gackstatter R (1985) The flow over two-dimensional surface-mounted obstacles at low Reynolds numbers. *J Fluids Eng* 107:489–494. <https://doi.org/10.1115/1.3242518>
- Tzeng SC, Ma WP, Wang YC (2007) Friction and forced convective heat transfer in a sintered porous channel with obstacle blocks. *Heat Mass Transf Und Stoffuebertragung* 43:687–697. <https://doi.org/10.1007/S00231-006-0149-Z/TABLES/5>
- Warrier P, Sathyanarayana A, Patil DV et al (2012) Novel heat transfer fluids for direct immersion phase change cooling of electronic systems. *Int J Heat Mass Transf* 55:3379–3385. <https://doi.org/10.1016/J.IJHEATMASSTRANSFER.2012.02.063>
- Xie WA, Xi GN, Zhong MB (2017) Effect of the vortical structure on heat transfer in the transitional flow over a backward-facing step. *Int J Refrig* 74:465–474. <https://doi.org/10.1016/J.IJREFRIG.2016.11.001>
- Xing H, Du W, Sun P et al (2022) Influence of surface curvature and jet-to-surface spacing on heat transfer of impingement cooled turbine leading edge with crossflow and dimple. *Int Commun Heat Mass Transf* 135:106116. <https://doi.org/10.1016/J.ICHEA.TMASSTRANSFER.2022.106116>
- Yan Y, Zhang C, Gao J et al (2021) Numerical study on premixed hydrogen/air combustion characteristics and heat transfer enhancement of micro-combustor embedded with pin fins. *Int J Hydrogen Energy* 46:38519–38534. <https://doi.org/10.1016/J.IJHYDENE.2021.09.097>
- Yojina J, Ngamsaad W, Nuttavut N et al (2010) Investigating flow patterns in a channel with complex obstacles using the lattice Boltzmann method. *J Mech Sci Technol* 24:2025–2034. <https://doi.org/10.1007/s12206-010-0712-x>
- Zeeshan A, Hassan M, Ellahi R, Nawaz M (2016) Shape effect of nanosize particles in unsteady mixed convection flow of nanofluid over disk with entropy generation: 231: 871–879. <https://doi.org/10.1177/0954408916646139>
- Zhang C, Yan Y, Shen K et al (2022) Numerical study on combustion characteristics and heat transfer enhancement of the micro

combustor embedded with Y-shaped fin for micro thermo-photovoltaic system. *Appl Therm Eng* 211:118427. <https://doi.org/10.1016/J.APPLTHERMALENG.2022.118427>

Zhou Y, Chen B, Chen W et al (2022) A novel opposite sinusoidal wave flow channel for performance enhancement of proton exchange membrane fuel cell. *Energy* 261:125383. <https://doi.org/10.1016/J.ENERGY.2022.125383>

Springer Nature or its licensor (e.g. a society or other partner) holds exclusive rights to this article under a publishing agreement with the author(s) or other rightsholder(s); author self-archiving of the accepted manuscript version of this article is solely governed by the terms of such publishing agreement and applicable law.